

Chaos and wild chaos in Lorenz-type systems

Hinke M. Osinga, Bernd Krauskopf and Stefanie Hittmeyer

Abstract This contribution provides a geometric perspective on the type of chaotic dynamics that one finds in the original Lorenz system and in a higher-dimensional Lorenz-type system. The latter provides an example of a system that features robust homoclinic tangencies; one also speaks of ‘wild chaos’ in contrast to the ‘classical chaos’ where homoclinic tangencies can only occur densely, and not robustly in open intervals in parameter space. Specifically, we discuss the manifestation of chaotic dynamics in the three-dimensional phase space of the Lorenz system, and illustrate the geometry behind the process that results in its description by a one-dimensional noninvertible map. For the higher-dimensional Lorenz-type system, the corresponding reduction process leads to a two-dimensional noninvertible map introduced in 2006 by Bamón, Kiwi, and Rivera-Letelier [arXiv 0508045] as a system displaying wild chaos. We present the geometric ingredients — in the form of different types of tangency bifurcations — that one encounters on the route to wild chaos.

1 Introduction

The Lorenz system was introduced and studied by meteorologist Edward Lorenz in the 1960s as an extremely simplified model for atmospheric convection dynamics

Hinke M. Osinga

Department of Mathematics, The University of Auckland, Private Bag 92019, Auckland 1142, New Zealand, e-mail: h.m.osinga@auckland.ac.nz

Bernd Krauskopf

Department of Mathematics, The University of Auckland, Private Bag 92019, Auckland 1142, New Zealand, e-mail: b.krauskopf@auckland.ac.nz

Stefanie Hittmeyer

Department of Mathematics, The University of Auckland, Private Bag 92019, Auckland 1142, New Zealand, e-mail: stefanie.hittmeyer@auckland.ac.nz

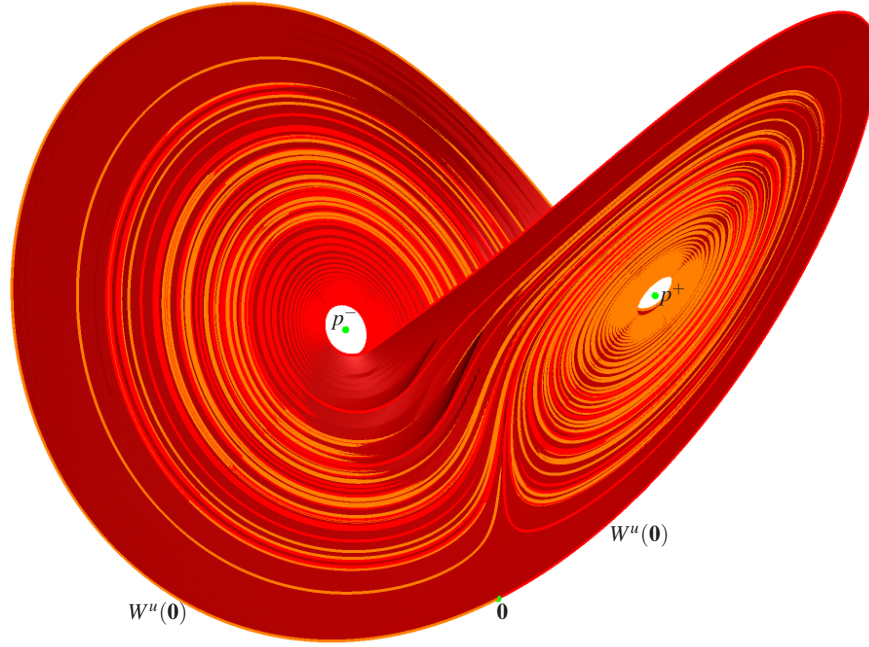


Fig. 1 The Lorenz attractor as computed and rendered as a surface, with the equilibria $\mathbf{0}$ and p^\pm and the manifold $W^u(\mathbf{0})$.

[35]. Famously, Lorenz discovered sensitive dependence on the initial condition, and the Lorenz system has arguably become the best-known example of a chaotic system. It is given as the vector field

$$\begin{cases} \dot{x} = \sigma(y - x), \\ \dot{y} = \rho x - y - xz, \\ \dot{z} = -\beta z + xy. \end{cases} \quad (1)$$

The system is invariant under the symmetry of a rotation about the z -axis by π . The now classical choice of the parameters for which Lorenz found a chaotic attractor is

$$\sigma = 10, \quad \rho = 28, \quad \beta = 2\frac{2}{3}. \quad (2)$$

For these parameters, (1) has three equilibria: the origin $\mathbf{0}$ and a symmetrically related pair of secondary equilibria p^\pm , which are all saddles. The chaotic attractor is often called the Lorenz or butterfly attractor. It has two ‘wings,’ which are centred at p^- and p^+ (which are not part of the attractor). Importantly, the Lorenz attractor contains $\mathbf{0}$ and its one-dimensional unstable manifold $W^u(\mathbf{0})$, that is, the two trajectories that converge to $\mathbf{0}$ in backward time. The Lorenz attractor actually consists of infinitely many layers or sheets that are connected along $W^u(\mathbf{0})$, which forms the

‘outer boundary’ of the attractor. This is already sketched and studied in the original paper by Lorenz [35]; an illustration of the different layers of the Lorenz attractor can be found in the paper by Perelló [40] and it is reproduced in [14].

Figure 1 shows a computed version of the Lorenz attractor, which was rendered as a surface from computed orbit segments of several suitably chosen families; see [14] for detail of this computation. Also shown in Figure 1 is the one-dimensional unstable manifold $W^u(\mathbf{0})$, with its left and right branches rendered in different shades; observe how $W^u(\mathbf{0})$ forms the outer boundary of the Lorenz attractor. Our visualisation in Figure 1 is quite different from most images of the Lorenz attractor that are obtained with numerical simulation. Starting from some initial condition, and letting transients die down, the Lorenz attractor is typically visualised by plotting (a long part of) the remaining trajectory. In this way, the part of the Lorenz attractor closest to the origin is generally missed, as it is not ‘visited’ very often by trajectories; hence, most published images show a considerably smaller part of the Lorenz attractor.

The Lorenz system (1) has been studied since the 1970s via the concept of the *geometric Lorenz attractor*, which is an abstract geometric model introduced by Guckenheimer [24], Guckenheimer and Williams [26], and Afrajmovich, Bykov and Shilnikov [1, 2]; see also [8, 44]. The key is that the geometric Lorenz attractor displays all the features observed in the Lorenz system, and that it can be reduced rigorously to a one-dimensional noninvertible map. This reduction is done in two steps. First of all, one considers the Poincaré return map to the horizontal section through the points p^\pm (given by $z = \rho - 1$). Locally this map is a diffeomorphism that has a stable foliation (near the classic parameter values), that is, an invariant foliation that is uniformly contracted by the Poincaré return map. The map on the quotient space of this foliation is a one-dimensional noninvertible map, called the *Lorenz map*, and it describes the dynamics on the geometric Lorenz attractor exactly. It can be shown with standard methods that the Lorenz map has chaotic dynamics; see, for example, [25]. In 1999 Tucker [45] famously provided a computer-assisted proof that, for the classical parameter values (2), the Lorenz system (1) satisfies the technical conditions of this geometric construction, thereby showing that the Lorenz attractor is indeed a chaotic attractor.

The question how chaos arises in the Lorenz system has also been considered, where ρ is chosen traditionally as the parameter that is varied [15, 43]. For small $\rho > 1$ all typical initial conditions simply end up at either p^- or p^+ , which are the only attractors of (1). As ρ is increased, a first homoclinic bifurcation at $\rho \approx 13.9265$ is encountered; here both branches of the one-dimensional unstable manifold $W^u(\mathbf{0})$ of the origin return to $\mathbf{0}$ to form a pair of homoclinic connections. This global bifurcation creates not only a pair of (symmetrically related) saddle periodic orbits, but also a hyperbolic set of saddle type. The result is what has been called preturbulence [29], which is characterised by the existence of arbitrarily long chaotic transients before the system settles down to either p^- or p^+ (still the only attractors). At $\rho \approx 24.0579$ one encounters a pair of heteroclinic cycles between the origin and the pair of saddle periodic orbits, and this results in the creation of a chaotic attractor. The chaotic attractor, which is the closure of $W^u(\mathbf{0})$, coexists with the two stable equilibria until

they become saddles in a Hopf bifurcation at $\rho = 470/19 \approx 24.7368$. After the Hopf bifurcation and up to $\rho = 28$, the chaotic attractor is the only attractor.

A crucial role in the organisation of the dynamics of the Lorenz system (1) is played by the stable manifold $W^s(\mathbf{0})$ of the origin $\mathbf{0}$, which we refer to as the Lorenz manifold. The origin $\mathbf{0}$ is a saddle equilibrium (for $\rho > 1$) with two stable directions and one unstable direction, and $W^s(\mathbf{0})$ is a smooth surface that consists of all points in \mathbb{R}^3 that end up at $\mathbf{0}$. Before the first homoclinic bifurcation, $W^s(\mathbf{0})$ forms the boundary between the two attractors p^- and p^+ . In the preturbulent regime after the first homoclinic bifurcation $W^s(\mathbf{0})$ is still part of the basin boundary of p^\pm , but it is much more complicated topologically as it is involved in organising arbitrarily long transients.

More importantly for the purpose of this paper, the Lorenz manifold $W^s(\mathbf{0})$ organises the dynamics in the chaotic regime [14, 15]. Owing to the sensitive dependence on the initial condition, $W^s(\mathbf{0})$ is dense in phase space. Moreover, the interaction of the Lorenz manifold $W^s(\mathbf{0})$ with the unstable manifold $W^u(\mathbf{0})$ gives rise to infinitely many further homoclinic bifurcations when ρ is varied. Closely related is the fact that there are infinitely many homoclinic tangencies between the two-dimensional stable and unstable manifolds of the saddle periodic orbits that lie dense in the chaotic Lorenz attractor. More generally, such tangencies of a three-dimensional vector field correspond directly (by taking a Poincaré return map) to homoclinic tangencies of the one-dimensional stable and unstable manifolds of fixed or periodic points of a planar diffeomorphism such as the Hénon map [27], which is another well-known chaotic system. Near a homoclinic tangency one can construct Smale horseshoe dynamics, that is, a chaotic hyperbolic set of saddle type. Moreover, any homoclinic tangency of a one-parameter family of three-dimensional vector fields, or planar diffeomorphisms, is accumulated in parameter space by other homoclinic tangencies [39], leading to an infinite sequence of homoclinic tangency points accumulating on other homoclinic tangency points. This is one of the characterizing properties of ‘classical chaos’ that arises in vector fields of dimension three and in diffeomorphisms of dimension two, for which the Lorenz system and the Hénon map are standard examples; see, for example, textbooks such as [4, 25, 42].

At a homoclinic tangency of a hyperbolic set (such as a periodic orbit) there is a nontransversal intersection of its stable and unstable manifolds. In particular, the point of homoclinic tangency is nonwandering and its tangent bundle cannot be decomposed into stable and unstable subspaces. As a result, the system is not uniformly hyperbolic, or simply, it is *nonhyperbolic* at a homoclinic tangency. In other words, in ‘classical chaos’ one finds infinitely many accumulating points of nonhyperbolicity. A property is said to be *robust* (in the C^1 -topology) if there is an open neighbourhood in the space of vector fields or diffeomorphisms such that all these systems have said property. As it turns out, it has been argued that nonhyperbolicity and homoclinic tangencies do not occur *robustly* in three-dimensional vector fields or two-dimensional diffeomorphisms [36].

On the other hand, robust homoclinic tangencies and, hence, robust nonhyperbolicity can be found in vector fields of dimension at least four and in diffeomorphisms of dimension at least three [11]. Any system with this property is said to

display *wild chaos* [37]. There are several constructions of diffeomorphisms that feature robust nonhyperbolicity [3, 6, 7, 21, 22]. Moreover, in [49] it is shown that a four-dimensional vector field model of calcium dynamics in a neuronal cell has a heterodimensional cycle between two saddle periodic orbits, which is directly associated with robust hyperbolicity [11, 29]. It is also possible to construct an n -dimensional vector field with robust homoclinic tangencies of a singular attractor and, hence, with wild chaos. Turaev and Shilnikov presented such an example for $n \geq 4$ in [46, 47]. We consider here the example for $n \geq 5$ due to Bamón, Kiwi, and Rivera-Letelier [9], which is constructed as a Lorenz-type system. It suffices to consider their construction for $n = 5$; the associated attractor is called *Lorenz-like* because it is effectively a higher-dimensional version of the geometric Lorenz-attractor. The dynamics of the five-dimensional Lorenz-type vector field is described by a four-dimensional diffeomorphism given as the Poincaré return map to a suitable codimension-one section. On this section there is a two-dimensional stable foliation, and the resulting quotient map is now a noninvertible map of the plane. This map is given in [9] in explicit form; in fact, Bamón, Kiwi, and Rivera-Letelier construct their example by starting from the noninvertible map, lifting it to the four-dimensional Poincaré return map and then suspending this diffeomorphism to obtain an abstract five-dimensional Lorenz-type vector field. In a small neighbourhood of a specific point in parameter space, they then show that the planar noninvertible map is robustly nonhyperbolic.

The goal of this paper is to determine and illustrate the geometry behind chaos in the Lorenz system and wild chaos in the five-dimensional Lorenz-type system. This study is made possible by advanced numerical methods — based on solving families of boundary value problems — for the computation of two-dimensional global manifolds of vector fields [15, 30, 31, 33] and tangency bifurcations involving stable and unstable sets of noninvertible planar maps [10, 28]; their implementation is done in the packages AUTO [13] and Cl_MatContM [18, 23], respectively. Section 2 is concerned with the Lorenz system. Our starting point in Section 2.1 is the discussion of how the three-dimensional phase space is organised globally by the two-dimensional Lorenz manifold $W^s(\mathbf{0})$ of the origin in the presence of the classical Lorenz attractor. We then discuss in Section 2.2 the geometry behind the description of the dynamics on the Lorenz attractor by the one-dimensional Lorenz map. The two-dimensional Lorenz-like map is introduced in Section 3 and its basic properties are discussed. The transition from simple to wild chaos is the subject of Section 3.1, where we show how different types of tangency bifurcations are involved in creating increasingly complicated dynamics. In Section 3.2 we present a two-parameter bifurcation diagram with curves of the different tangency bifurcations, which allows us to identify a large region where we conjecture wild chaos to be found. Finally, Section 4 summarises the results and briefly discusses avenues for future research.

2 Chaos in the Lorenz system

In this section we consider the chaotic dynamics of the Lorenz system (1) for the classical parameter values given in (2). We first consider the organisation of the full phase space and then illustrate the geometry behind the reduction to the one-dimensional Lorenz map.

2.1 Global organisation of the phase space

The Lorenz attractor is the only attractor of (1) for $\rho = 28$. Its basin is the entire phase space \mathbb{R}^3 with the exception of the symmetric pair of secondary equilibria p^\pm and their one-dimensional stable manifolds $W^s(p^\pm)$. Recall that the origin $\mathbf{0}$ and its one-dimensional unstable manifold $W^u(\mathbf{0})$ are part of the chaotic attractor. This also means that the two-dimensional stable manifold $W^s(\mathbf{0})$ lies in the basin of the Lorenz attractor. Moreover, locally near $\mathbf{0}$ the invariant surface $W^s(\mathbf{0})$ determines the dynamics in the following sense: initial conditions on one side of $W^s(\mathbf{0})$ flow away from the origin into the left wing of the attractor (towards negative values of x) and those on the other side flow away from the origin into the right wing of the attractor (towards positive values of x). The sensitive dependence on initial conditions of the dynamics on the Lorenz attractor has global consequences throughout the phase space. Any open sphere in phase space, no matter how small, must contain two points that eventually move over the Lorenz attractor differently: at some point in time one trajectory is, say, on the left wing, while the other is on the right wing. This means that, locally near the attractor, the two trajectories are on either side of $W^s(\mathbf{0})$. This implies that $W^s(\mathbf{0})$ must divide the open sphere into two open halves, each containing one of the two initial conditions. In turn this proves that $W^s(\mathbf{0})$ lies dense in the basin of the Lorenz attractor and, hence, also in \mathbb{R}^3 .

According to the stable and unstable manifold theorem [38], locally near $\mathbf{0}$ the surface $W^s(\mathbf{0})$ is a small topological disk that is tangent to the two-dimensional stable linear eigenspace $E^s(\mathbf{0})$ spanned by the eigenvectors of the two negative real eigenvalues. This disk can be imagined to grow while its boundary maintains a fixed geodesic distance (distance of the shortest path on $W^s(\mathbf{0})$) to the origin $\mathbf{0}$. At any stage of this growth process one is dealing with a smooth embedding of the standard unit disk into \mathbb{R}^3 yet, as it grows, this topological disk fills out \mathbb{R}^3 densely. Hence, loosely speaking, one can imagine the surface $W^s(\mathbf{0})$ as a growing, space-filling pancake.

We developed a numerical method for the computation of two-dimensional stable and unstable manifolds, called the geodesic level set (GLS) method [30]. This method is based on the idea of growing such a manifold by adding geodesic bands to it at each step. With the GLS method we are able to compute a first part of $W^s(\mathbf{0})$ as a surface up to a considerable geodesic distance. On the other hand, in order to examine the denseness of $W^s(\mathbf{0})$ in \mathbb{R}^3 a different approach is needed. Namely, we consider the intersection set $\widehat{W}^s(\mathbf{0}) := W^s(\mathbf{0}) \cap S_R$ with a suitable chosen sphere S_R ,

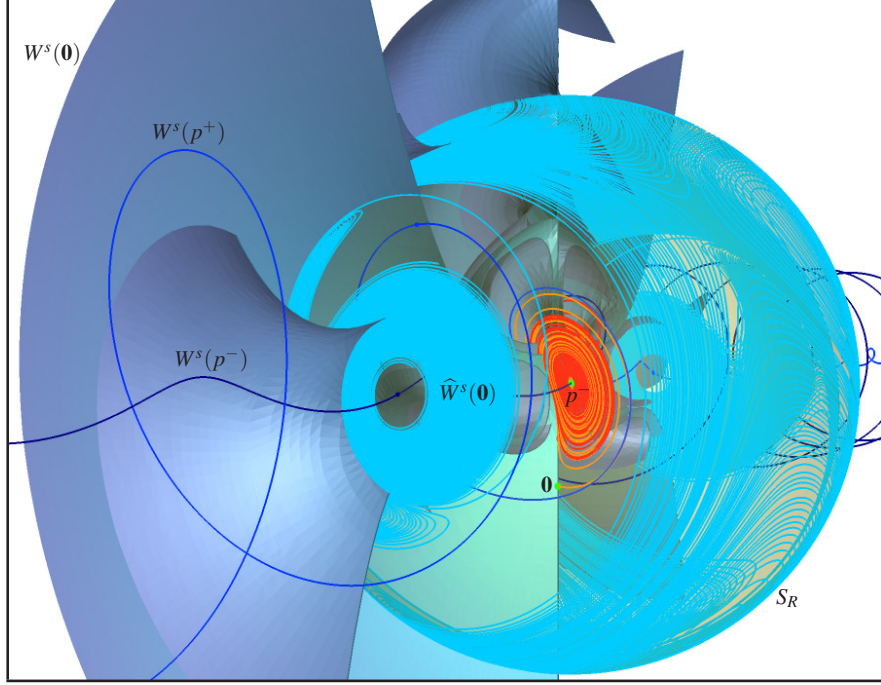


Fig. 2 The Lorenz manifold $W^s(\mathbf{0})$ for $\rho = 28$ intersecting the sphere S_R with $R = 70.7099$ in the set $\hat{W}^s(\mathbf{0})$; also shown are the equilibria $\mathbf{0}$ and p^- and the one-dimensional manifolds $W^u(\mathbf{0})$ and $W^s(p^\pm)$.

which is then computed directly by defining a boundary value problem such that its solutions are orbit segments with begin point on S_R and end point in $E^s(\mathbf{0})$ near $\mathbf{0}$; see [5, 15] for details. More specifically, we choose the centre of S_R as the point $(0, 0, \rho - 1)$ on the z -axis, which lies exactly in the middle of the line that connects the two equilibria p^\pm . The radius R of S_R is chosen such that the Lorenz attractor is well inside S_R , and the second intersection points in $\hat{W}^s(p^\pm) := W^s(p^\pm) \cap S_R$ of the small-amplitude branches of $W^s(p^\pm)$ lie on the ‘equator’ of S_R — for $\rho = 28$ as considered here, this gives $R = 70.7099$; see [15] for details.

Figure 2 illustrates the geometry of how $W^s(\mathbf{0})$ intersects the sphere S_R . The view is from a point with negative x - and y -coordinates, and only one half of the computed part of the surface $W^s(\mathbf{0})$ is shown, namely, the part with $y \geq 0$. The sphere S_R is rendered transparent. Inside S_R , we can clearly see the equilibria $\mathbf{0}$ and p^- , with p^+ obscured by $W^s(\mathbf{0})$. The one-dimensional unstable manifold $W^u(\mathbf{0})$, with its left and right branches rendered in different shades, gives an idea of the location of the Lorenz attractor. Also shown in Figure 2 are the two one-dimensional stable manifolds $W^s(p^\pm)$, each drawn in different shades. Note that the small-amplitude branch of $W^s(p^-)$ indeed intersects S_R along its equator, while the large-amplitude branch of $W^s(p^+)$ intersects S_R at a point higher up and closer to the z -axis. Recall

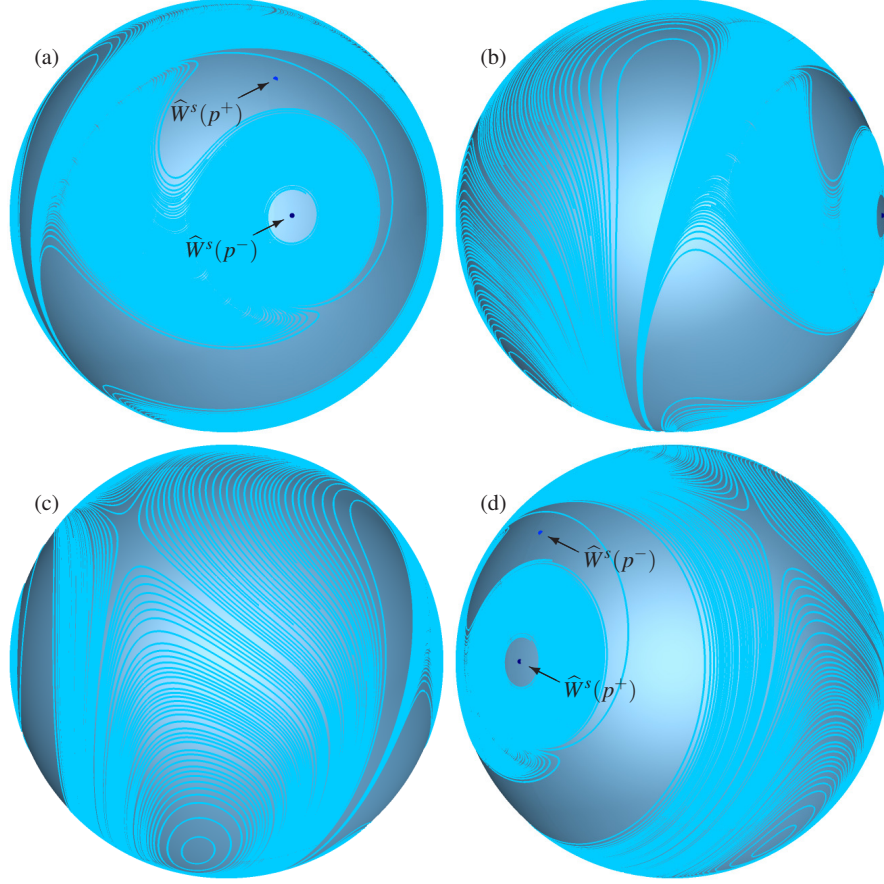


Fig. 3 The set $\widehat{W}^s(\mathbf{0})$ for $p = 28$ on the sphere S_R with $R = 70.7099$; also shown are $\widehat{W}^s(p^\pm)$.

that $p^\pm \cup W^s(p^\pm)$ forms the complement of the basin of the Lorenz attractor. The surface $W^s(\mathbf{0})$ can be seen to wrap around the curves $W^s(p^\pm)$, which it cannot intersect. The part of $W^s(\mathbf{0})$ that is shown, which was computed up to geodesic distance 162.5, generates the beginnings of what appear to be only three intersection curves in $\widehat{W}^s(\mathbf{0})$. It is clear that an impractically large piece of $W^s(\mathbf{0})$ would need to be computed to generate the many curves in $\widehat{W}^s(\mathbf{0})$ that are shown in Figure 2; this is why $\widehat{W}^s(\mathbf{0})$ is computed directly.

Figure 3 shows four different views of the the computed intersection curves in $\widehat{W}^s(\mathbf{0})$ on the sphere S_R ; also shown on S_R are the points in $\widehat{W}^s(p^\pm)$. In all views, the vertical axis is the z -axis of (1). In Figure 3(a), the horizontal axis is the direction defined by $(\cos \theta, -\sin \theta)$, with $\theta = 3\pi/10$ (in other words, the (x, y) -plane was rotated clockwise by $3\pi/10$ about the z -axis). The view points in panels (b)–(d) are consecutively rotated by a further $\pi/4$ radians about the z -axis; note that a further rotation over $\pi/4$ would show the symmetrical version of Figure 3(a) with

$\widehat{W}^s(p^-)$ and $\widehat{W}^s(p^+)$ interchanged. Figure 3 is designed to illustrate how $W^s(\mathbf{0})$ fills the phase space \mathbb{R}^3 by showing the intersection set $\widehat{W}^s(\mathbf{0})$ on the sphere S_R . Notice the intricate structure of how the curves in $\widehat{W}^s(\mathbf{0})$ fill up S_R ; see also [15]. As one might expect, the computed curves in $\widehat{W}^s(\mathbf{0})$ are not distributed evenly on S_R , and there are several larger regions on S_R without computed curves in $\widehat{W}^s(\mathbf{0})$. This is due to the fact that a finite computation is performed to show an infinite process. More specifically, the curves in $\widehat{W}^s(\mathbf{0})$ that are shown in Figure 3 have the property that the overall integration time of the associated computed orbit segments is no larger than 7.0; see [15] for details of the computational setup. This bound already leads to a considerable computation generating 350 MB of AUTO data and 377 individual curves in $\widehat{W}^s(\mathbf{0})$. As we have checked, these regions fill up with additional curves in $\widehat{W}^s(\mathbf{0})$ if one allows for a larger bound on the integration time of orbit segments; however, the number of curves thus obtained and, hence, the duration and data produced grow exponentially with the bound on the integration time. Figure 3 provides a good illustration of the space-filling nature of the surface $W^s(\mathbf{0})$ in phase space that, in turn, constitutes a global geometric interpretation of the sensitive dependence of the Lorenz system (1) on the initial conditions.

2.2 From Lorenz attractor to Lorenz map

The first step in the reduction process resulting in the description of the dynamics on the Lorenz attractor by the Lorenz map is to consider the Poincaré return map to the horizontal plane Σ_ρ through the secondary equilibria p^\pm , which is given by

$$\Sigma_\rho := \{(x, y, z) \in \mathbb{R}^3 \mid z = \rho - 1\}. \quad (3)$$

Geometrically, this means that one needs to consider the intersection sets with Σ_ρ of the relevant invariant objects of the vector field (1). Figure 4 illustrates the situation. The Lorenz attractor, represented by the unstable manifold $W^u(\mathbf{0})$ accumulating on it, can be found in the middle of the image. It is intersected by Σ_ρ , which is rendered transparent, at the height of the equilibria p^\pm . The stable manifold $W^s(\mathbf{0})$ is shown as computed up to geodesic distance 162.5; the parts of $W^s(\mathbf{0})$ below and above the plane Σ_ρ are rendered solid and transparent, respectively. The outer boundary of the computed part of $W^s(\mathbf{0})$ (the geodesic level set of geodesic distance 162.5) is highlighted to help illustrate the complicated geometry of this surface, which is topologically a disk. The surface $W^s(\mathbf{0})$ can be seen in Figure 4 to intersect Σ_ρ in several curves of the set $\overline{W}^s(\mathbf{0}) := W^s(\mathbf{0}) \cap \Sigma_\rho$. One of them is the primary intersection curve $\overline{W}_0^s(\mathbf{0})$, which is invariant under the symmetry of a rotation by π about the z -axis and contains the point $(0, 0, \rho - 1)$. Also shown in Figure 4 are the one-dimensional manifolds $W^s(p^\pm)$, which intersect Σ_ρ in discrete points.

It is important to realise, as can easily be checked from (1), that the flow is tangent to Σ_ρ along the *tangency locus*

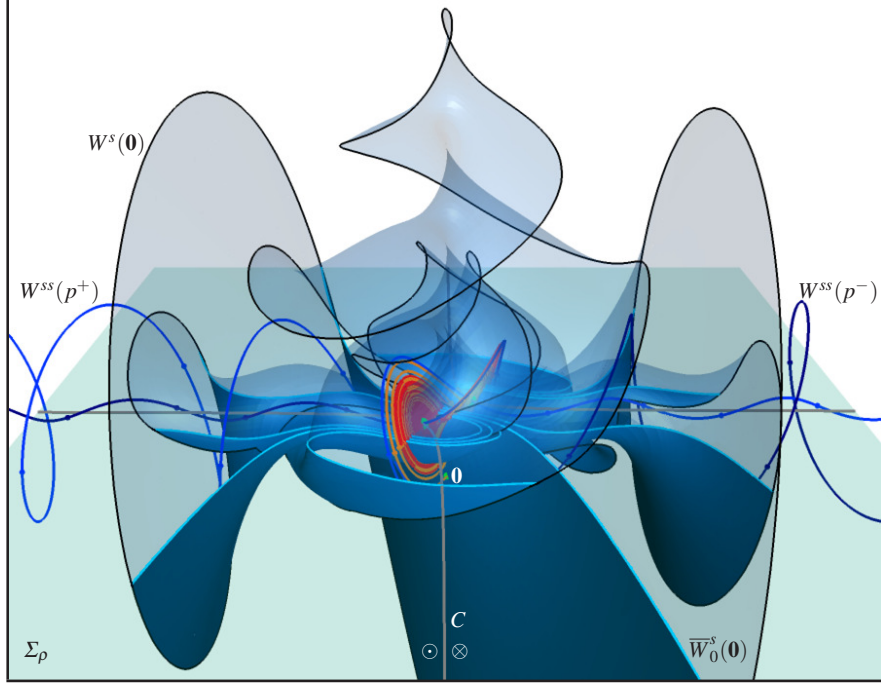


Fig. 4 The manifold $W^s(\mathbf{0})$ for $\rho = 28$ computed up to geodesic distance 162.5 and its intersection with the plane Σ_ρ ; the section Σ_ρ and the part of $W^s(\mathbf{0})$ above it are rendered transparent. Also shown are the equilibria $\mathbf{0}$ and p^\pm , the one-dimensional manifolds $W^u(\mathbf{0})$ and $W^s(p^\pm)$, and the tangency locus C on Σ_ρ .

$$C = \{(x, y, \rho - 1) \in \mathbb{R}^3 \mid xy = \beta(\rho - 1)\}. \quad (4)$$

The set C consists of two hyperbolas, which contain the equilibria $p^\pm \in \Sigma_\rho$, respectively. In between the two hyperbolas the vector field points downward (towards negative z), which is indicated by the symbol \otimes in Figure 4. In the regions to the other side of C the vector field points upward (towards positive z), which is indicated by the symbol \odot . As a result, the Poincaré return map, defined as the first return to the section, is not a diffeomorphism on the entire plane Σ_ρ . This is why one defines the local Poincaré return map only on the central region of Σ_ρ where the direction of the flow is downward [24], that is, in between the two hyperbolas of C ; technically, this means that one considers the second return to Σ_ρ .

However, this local Poincaré map on the central region is still not a diffeomorphism. Namely, points along the primary intersection curve $\bar{W}_0^s(\mathbf{0})$ converge to $\mathbf{0} \notin \Sigma_\rho$ under the flow and, hence, do not return to the section Σ_ρ . This means that the Poincaré map is not defined on $\bar{W}_0^s(\mathbf{0})$. Trajectories through points to the left of $\bar{W}_0^s(\mathbf{0})$ spiral around p^- before intersecting Σ_ρ again, while those through points to the right of $\bar{W}_0^s(\mathbf{0})$ spiral around p^+ before intersecting the central region of Σ_ρ .

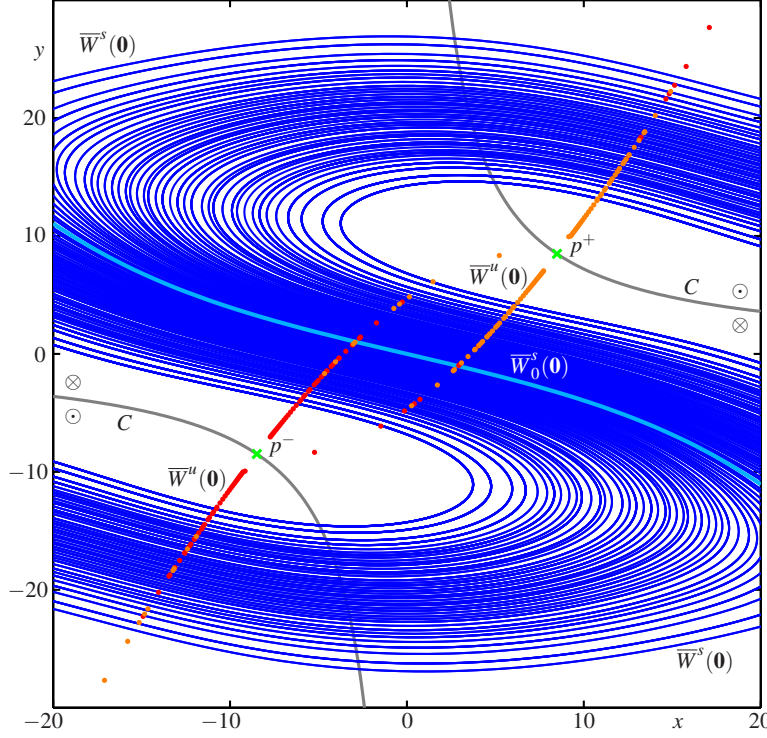


Fig. 5 The invariant objects of (1) for $\rho = 28$ in the plane Σ_ρ ; compare with Figure 4. Shown are the equilibria p^\pm , the tangency locus C , the intersection set of the Lorenz attractor as represented by $\bar{W}^u(\mathbf{0})$, and curves in $\bar{W}^s(\mathbf{0})$; the primary intersection curve $\bar{W}_0^s(\mathbf{0})$ is highlighted, and it divides the central region labelled \otimes where the direction of the flow is downward.

again. Hence, the local Poincaré map has a discontinuity across the curve $\bar{W}_0^s(\mathbf{0})$, and it maps each of the two complementary regions either side of $\bar{W}_0^s(\mathbf{0})$ over the entire central region between the two hyperbolas in C .

Figure 5 shows the respective invariant objects in the plane Σ_ρ , which can be identified with the (x, y) -plane (with fixed $z = \rho - 1$). By construction, the equilibria p^\pm lie in Σ_ρ and on the tangency locus C that bound the central region indicated by the symbol \otimes . The Lorenz attractor is represented by the intersection points $\bar{W}^u(\mathbf{0}) := W^u(\mathbf{0}) \cap \Sigma_\rho$ of the unstable manifold $W^u(\mathbf{0})$. These intersection points appear to intersect Σ_ρ in four disjoint curves, two of which lie in the central region; note that the Lorenz attractor does not contain the points p^\pm and compare with Figure 1. Also shown in Figure 5 are many curves of the intersection set $\bar{W}^s(\mathbf{0})$, and the primary curve $\bar{W}_0^s(\mathbf{0})$ is highlighted. Curves in the set $\bar{W}^s(\mathbf{0})$ were computed directly by imposing the boundary condition that the corresponding orbit segments have their begin point in Σ_ρ ; by contrast, in Figure 4 the shown curves in $\bar{W}^s(\mathbf{0})$ were obtained from the computed part of the two-dimensional manifold $W^s(\mathbf{0})$.

The reduction of the Poincaré map to the Lorenz map for $\rho = 28$ relies on the fact that the geometric Lorenz system — the abstract version of the Lorenz system — admits an invariant stable foliation in some neighbourhood of the chaotic attractor [1, 26, 41, 48]. This means that leaves of this foliation are mapped to leaves, and the dynamics on the leaves is a contraction. When restricted to said neighbourhood of the attractor, the curves in $\overline{W}^s(\mathbf{0})$ generate the stable foliation by means of taking their closure. Hence, Figure 5 provides an illustration of the stable foliation by showing a large number of curves in $\overline{W}^s(\mathbf{0})$. The leaves of this foliation intersect the segment of the diagonal between p^- and p^+ in unique points. The one-dimensional Lorenz map is defined on this diagonal segment — or, rather, on the corresponding interval of the variable x — and it describes how leaves are mapped to leaves under the Poincaré map on the central region of Σ_ρ . The Lorenz map is topologically conjugate to the map

$$x \mapsto \begin{cases} 1 - \beta |x|^\alpha, & x \in [-1, 0), \\ -1 + \beta |x|^\alpha, & x \in (0, 1], \end{cases} \quad (5)$$

with $0 < \alpha < 1$, $\beta \in (1, 2)$ and $\alpha\beta > 1$; see [25]. Here, α is the ratio between the magnitudes of the weak stable and unstable eigenvalues of the equilibrium $\mathbf{0}$ of the Lorenz system (1). The Lorenz map is not invertible because it maps the subinterval $[-1, 0)$ to a much larger subinterval in $[-1, 1]$; due to symmetry, the same is true for the subinterval $(0, 1]$. Moreover, the Lorenz map has a discontinuity at 0, which is also referred to as the *critical point*; note that 0 corresponds to the point $(0, 0, \rho - 1) \in \overline{W}^s(\mathbf{0})$ that never returns to Σ_ρ . The critical point 0 has infinitely many preimages under the Lorenz map, because all points on $\overline{W}^s(\mathbf{0})$ eventually map to 0; compare with Figure 5. One can also take the point of view that the critical point 0 of the Lorenz map represents the origin $\mathbf{0}$ of the Lorenz system; then the (symmetrically related) first intersection points of $\overline{W}^u(\mathbf{0})$ in the central region of Σ_ρ can be thought of as the forward (set-valued) image of the critical point 0. In particular, whenever these two points map to the critical point 0 under some iterate of the Lorenz map then this corresponds to a homoclinic orbit of $\mathbf{0}$ in the full Lorenz system.

The Lorenz map of the form (5) is a rigorous descriptions of the dynamics of the Lorenz system (1) provided that there is an invariant stable foliation. There is every indication that this is indeed the case in this entire ρ -range of $0 < \rho \leq 30.1$ [43]. Indeed, the Lorenz map has been used to study the (emergence of) chaotic dynamics for increasing ρ up to $\rho = 28$ [24, 29, 43]. On the other hand, it is known that for $\rho \geq 30.2$ the Lorenz system has ‘cusped horseshoes,’ the dynamics of which is definitely not represented faithfully by the one-dimensional Lorenz map [24, 43]. By which mechanism the stable foliation is lost near $\rho \approx 30.1$ is the subject of ongoing research [12].

A closely-related concept is the so-called Lorenz template [19, 20, 24, 35]. Geometrically, the Lorenz template is obtained from the Lorenz attractor in Figure 1 by the identification of points on the diagonal segment in between p^- and p^+ with points on the Lorenz attractor via the projection along leaves of the stable foliation

in Σ_ρ . More specifically, consider the points corresponding to the stable projections of the first intersection points of the two sides of $W^u(\mathbf{0})$ with Σ_ρ in the central region where the direction of the flow is downward. The diagonal segment connecting these two points contains the point $(0, 0, \rho - 1)$. Initial conditions on the diagonal segment on either side of $(0, 0, \rho - 1)$ sweep out two surfaces as the flow takes them around p^- and p^+ , respectively, until they return to the central region of Σ_ρ as two curves (that are very close to the intersection of the Lorenz attractor with Σ_ρ). Projection along stable leaves then identifies these two end curves with the initial diagonal segment. This segment can, hence, be thought of as the start and finish line on a branched two-manifold, that is, the topological object obtained by ‘glueing’ the two surfaces together along the diagonal in the central region of Σ_ρ ; this branched two-manifold is the Lorenz template. In particular, the Lorenz template allows one to describe the symbolic dynamics of the knot-types in \mathbb{R}^3 of periodic orbits in the Lorenz system [19]. Notice that the dynamics from start to finish on the Lorenz template is exactly given by the Lorenz map.

3 Wild chaos in a Lorenz-type system in dimension five

The reduction process for the three-dimensional (geometric) Lorenz system can also be applied to systems with phase-space dimension $n \geq 4$. In direct analogy, one obtains an invariant foliation in a suitable $(n - 1)$ -dimensional cross-section with leaves of codimension one and dimension $n - 2$; this would require that, near the Lorenz attractor, the additional directions are all stronger than those on the Lorenz attractor. Projection along stable leaves then results in a one-dimensional Lorenz map, meaning that the dynamics of such a vector field for $n \geq 4$ is just like that of the Lorenz system (1) itself.

To obtain a Lorenz-type vector field in higher dimensions with different dynamics from that of the Lorenz system (1), one needs to consider an example where the Poincaré map in a cross-section admits an invariant stable foliation of codimension at least two. In 2006, Bamón, Kiwi, and Rivera-Letelier [9] constructed such an abstract n -dimensional Lorenz-type vector field for $n \geq 5$ with a stable foliation of codimension two and dimension $n - 3$ in the $(n - 1)$ -dimensional cross-section; the minimal case $n = 5$ contains all the geometric ingredients, and we restrict to it for simplicity in the discussion that follows. The central object in [9] is the corresponding two-dimensional noninvertible quotient map, which is given on the punctured complex plane as

$$\begin{aligned} f : \mathbb{C} \setminus \{0\} &\rightarrow \mathbb{C} \\ z &\mapsto (1 - \lambda + \lambda |z|^a) \left(\frac{z}{|z|} \right)^2 + 1, \end{aligned} \tag{6}$$

with parameters $a, \lambda \in \mathbb{R}$ in the ranges $0 < a < 1$ and $0 < \lambda < 1$. Notice the term $|z|^a$, indicating a clear similarity with the form (5) of the one-dimensional Lorenz map.

A planar noninvertible map can have richer dynamics than a one-dimensional noninvertible map, where homoclinic tangencies can be at most dense in parameter space. Indeed, [9] provides a proof that there exists a small open region near the point $(a, \lambda) = (1, 1)$ in the (a, λ) -plane, such that the map (6) has a homoclinic tangency for every point from this parameter region; hence, homoclinic tangencies occur robustly, and the map, as well as the associated Lorenz-type vector field in \mathbb{R}^5 , exhibit wild chaos.

As is the case for the one-dimensional Lorenz map, the origin in \mathbb{C} does not have a well-defined image under (6). Hence, this point is a critical point, which we refer to as J_0 . The critical point J_0 arises, as in Section 2.2, from the fact that it lies on the three-dimensional stable manifold of an equilibrium e of the five-dimensional Lorenz-type vector field, where e does not lie in the cross-section on which the four-dimensional Poincaré map is defined. The equilibrium e has a two-dimensional unstable manifold that corresponds in the planar map (6) to the critical circle

$$J_1 = \{z \in \mathbb{C} \mid |z - 1| = 1 - \lambda\}, \quad (7)$$

with radius $1 - \lambda$ around the point $z = 1$. The equilibrium e plays the role of the origin $\mathbf{0}$ of the Lorenz system (1) and, in complete analogy, the critical circle J_1 can be interpreted as the set-valued image of the critical point J_0 . The map (6) maps the punctured complex plane $\mathbb{C} \setminus J_0$ in a two-to-one fashion — by angle doubling due to the term $(z/|z|)^2$ — to the region outside the circle J_1 ; the centre of the angle-doubling is shifted by 1 with respect to $J_0 = 0$. Dynamics and bifurcations of this type of map are the subject of [28], where we consider a more general family with an additional complex parameter c for the shift; it is set to $c = 1$ in (6) for simplicity and in accordance with the formulation of the map in [9].

Our goal here is to present geometric mechanisms that are involved in the transition from simple dynamics to wild chaos in the map (6) as the point $(a, \lambda) = (1, 1)$ is approached. Key ingredients in this transition are different types of global bifurcations. The map (6) has fixed points and periodic points, which correspond to periodic orbits of the associated vector field. If they are saddles then these points have stable and unstable invariant sets, which are the generalisations of stable and unstable manifolds to the context of noninvertible maps; see, for example, [16, 17, 32] for more details. Points on the stable set $W^s(p)$ of a saddle periodic point p converge to p under iteration of f^k where k is the (minimal) period of p ; note that $k = 1$ if p is a fixed point. Similarly, points on the unstable set $W^u(p)$ of p converge to p via a particular sequence of preimages of f^k . Note that $W^s(p)$ and $W^u(p)$ in the map (6) are one-dimensional objects, but they are typically not manifolds. The stable set $W^s(p)$ consists of a primary manifold $W_0^s(p)$ that contains p , and all preimages of $W_0^s(p)$, so that the stable set is typically a disjoint family of infinitely many one-dimensional manifolds. The unstable set may be an immersed one-dimensional manifold; however, sequence of preimages of points in $W^u(p)$ may not be unique,

in which case $W^u(p)$ has self-intersections. The stable and unstable sets of a saddle fixed or periodic point of the map (6) correspond to four-dimensional stable and two-dimensional unstable manifolds of the corresponding saddle periodic orbit in the five-dimensional Lorenz-type vector field.

Clearly, the stable and unstable sets of a fixed or periodic point p can become tangent, which is referred to as a *homoclinic tangency* and corresponds to a tangency between the respective manifolds of the associated periodic orbit in the five-dimensional Lorenz-type vector field. To characterise the additional global bifurcations that arise in the map (6) it is convenient to consider the *backward critical set*

$$\mathcal{J}^- := \cup_{k=0}^{\infty} f^{-k}(J_0)$$

of all preimages of the critical point J_0 , and the *forward critical set*

$$\mathcal{J}^+ := \cup_{k=0}^{\infty} f^k(J_1),$$

of all images of the critical circle J_1 . Note that \mathcal{J}^- consists of potentially infinitely many discrete points, while \mathcal{J}^+ consists of infinitely many closed curves; we refer to $\mathcal{J} = \mathcal{J}^- \cup \mathcal{J}^+$ as the *critical set*. With this notation, we can define three further tangency bifurcations: the *forward critical tangency* where a stable set $W^s(p)$ becomes tangent to the circles in the forward critical set \mathcal{J}^+ ; the *backward critical tangency* where a sequence of points in the backward critical set \mathcal{J}^- lies on an unstable set $W^u(p)$; and the *forward-backward critical tangency* where a sequence of points in the backward critical set \mathcal{J}^- lies on the forward critical set \mathcal{J}^+ . These three global bifurcation involving the critical set \mathcal{J} , as well as the homoclinic bifurcation, are encountered and discussed here as part of the transition to wild chaos. They are of codimension one, that is, they are encountered generically at isolated points when a single parameter is changed; their unfoldings are presented in detail in [28]. Note that a forward or backward critical tangency corresponds to a heteroclinic bifurcation between the corresponding periodic orbit and the equilibrium e of the Lorenz-type vector field. The forward-backward critical tangency, on the other hand, corresponds to the existence of an isolated homoclinic orbit of the saddle equilibrium e of the five-dimensional Lorenz-type vector field; it is the higher-dimensional analogue of how a homoclinic bifurcation in the Lorenz system (1) is described by the one-dimensional Lorenz map.

3.1 The transition for increasing $a = \lambda$

We now show a series of phase portraits as panels (a)–(l) of Figure 6 that illustrate the bifurcations that are encountered in the transition to wild chaos and generate the robustness of homoclinic tangencies; more specifically, we increase a and λ along the diagonal $a = \lambda$ towards the point $(a, \lambda) = (1, 1)$, near which wild chaos was proven to exist [9]. To facilitate the visualisations, we project the complex plane \mathbb{C} onto the Poincaré disk by stereographic projection, where the unit circle, that

is, the boundary of the Poincaré disk represents the directions to infinity. In each phase portrait we show a suitable number of points in the backward critical set \mathcal{J}^- (as dots) and the closed curves in the forward critical set \mathcal{J}^+ . We remark that the circle J_1 with radius $1 - \lambda$ appears distorted in all phase portraits as a result of stereographic projection. For the values $a, \lambda \in \mathbb{R}$ that we consider, the map (6) has one fixed point p on the positive real line and a complex-conjugate pair of fixed points q^\pm . We plot these fixed points p and q^\pm , as well as the stable set $W^s(p)$ and unstable set $W^u(p)$ of the saddle point p ; throughout, the points in \mathcal{J}^- are branch points of the stable set $W^s(p)$. Notice that all phase portraits are symmetric with respect to complex conjugation, owing to the fact that $a, \lambda \in \mathbb{R}$. The phase portraits in Figure 6 were obtained from computations of the transformed map on the Poincaré disk as follows: the fixed points p and q^\pm can be found readily; \mathcal{J}^- is represented by all backward images of J_0 under up to eleven backward iterations, that is, by $\cup_{k=0}^{11} f^{-k}(J_0)$; similarly, \mathcal{J}^+ is represented by J_1 and its next fourteen forward iterations; to obtain $W^s(p)$, we take advantage of the complex-conjugate symmetry and note that the primary manifold $W_0^s(p)$ is the real halfline $(0, \infty)$, which is the real interval $(0, 1]$ on the Poincaré disk; we computed eleven backward iterates of $W_0^s(p)$; finally, $W^u(p)$ was found by computing a first piece of arclength 5 and then plotting it and its next six iterates (in this way, we ensure that $W^u(p)$ maintains a suitable and comparable arclength as parameters are changed).

Figure 6(a) is for $a = \lambda = 0.7$, when the map (6) does not have chaotic dynamics, and all typical orbits converge to one of the two attracting fixed points q^\pm . The two branches of the unstable set $W^u(p)$ (which is an immersed manifold in this case) spiral towards q^+ and q^- , respectively. The preimages of $W_0^s(p)$ are organised in such a way that every point in the backward critical set \mathcal{J}^- connects four branches of $W^s(p)$. Moreover, \mathcal{J}^- accumulates on the boundary of the Poincaré disk. The forward critical set \mathcal{J}^+ , on the other hand, accumulates on the unstable set $W^u(p)$. Figure 6(b) shows the phase portrait for $a = \lambda = 0.72$, just after a Neimark-Sacker bifurcation (or Hopf bifurcation for maps) [34]. The fixed points q^\pm are now repellers and $W^u(p)$ and \mathcal{J}^+ accumulate on two invariant closed curves (not shown), which correspond to invariant tori in the associated Lorenz-type vector field. As a and λ change, these invariant closed curves undergo various bifurcations (associated with resonance phenomena) that we do not discuss here. Figure 6(c) shows the phase portrait for $a = \lambda = 0.73277$, approximately at the moment that $W^s(p)$ and $W^u(p)$ have a first homoclinic tangency. Since $W^u(p)$ accumulates on itself, this first homoclinic tangency is accumulated in parameter space, on the side of larger $a = \lambda$, by infinitely many homoclinic tangencies. As is shown in Figure 6(d) for $a = \lambda = 0.745$, after the first homoclinic tangency there is a homoclinic tangle between $W^s(p)$ and $W^u(p)$. Therefore, the system is now chaotic in the classical sense, meaning that any homoclinic tangency between $W^s(p)$ and $W^u(p)$ is accumulated by further homoclinic tangencies with associated saddle hyperbolic sets and horseshoe dynamics; see, for example, [11, 39]. Notice also that $W^s(p)$ accumulates on itself and the two branches of the unstable set $W^u(p)$ now intersect. Moreover, the forward critical set \mathcal{J}^+ accumulates on $W^u(p)$, so that the first homoclinic tangency is also accumulated in parameter space, on the side of larger $a = \lambda$, by

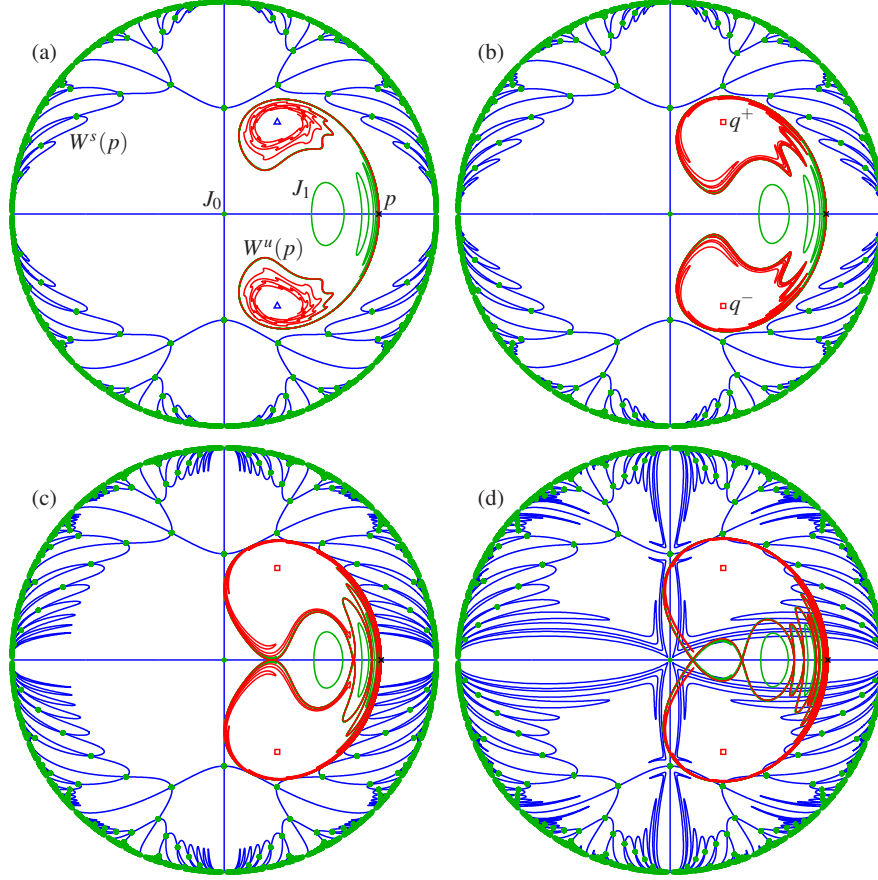


Fig. 6 The objects p (cross), q^\pm (triangles when attracting, and squares when repelling), $W^s(p)$, $W^u(p)$, \mathcal{J}^- and \mathcal{J}^+ on the Poincaré disk; from (a) to (d) $a = \lambda$ take the values 0.7, 0.72, 0.73277 and 0.745.

infinitely many forward critical tangencies; indeed, in Figure 6(d) there is a tangle between $W^s(p)$ and \mathcal{J}^+ as a result. Furthermore, the forward critical tangencies have the effect that the points in \mathcal{J}^- are branch points to infinitely many, instead of four branches of $W^s(p)$; see also [28]. In Figure 6(d), this can be seen at the origin, where an additional eight branches are shown to connect to 0; these are preimages of the two additional branches of $W^s(p)$ that intersect J_1 .

In Figure 6(e) for $a = \lambda = 0.76302$ one encounters the first backward critical tangency, where the unstable manifold $W^u(p)$ goes through the critical point $J_0 = 0$, which implies that $W^u(p)$ contains two sequences of preimages of J_0 (two because of symmetry). Since $W^u(p)$ accumulates on itself, this first backward critical tangency is accumulated in parameter space, on the side of larger $a = \lambda$, by infinitely many backward critical tangencies. Observe from Figure 6(f) for $a = \lambda = 0.765$ how

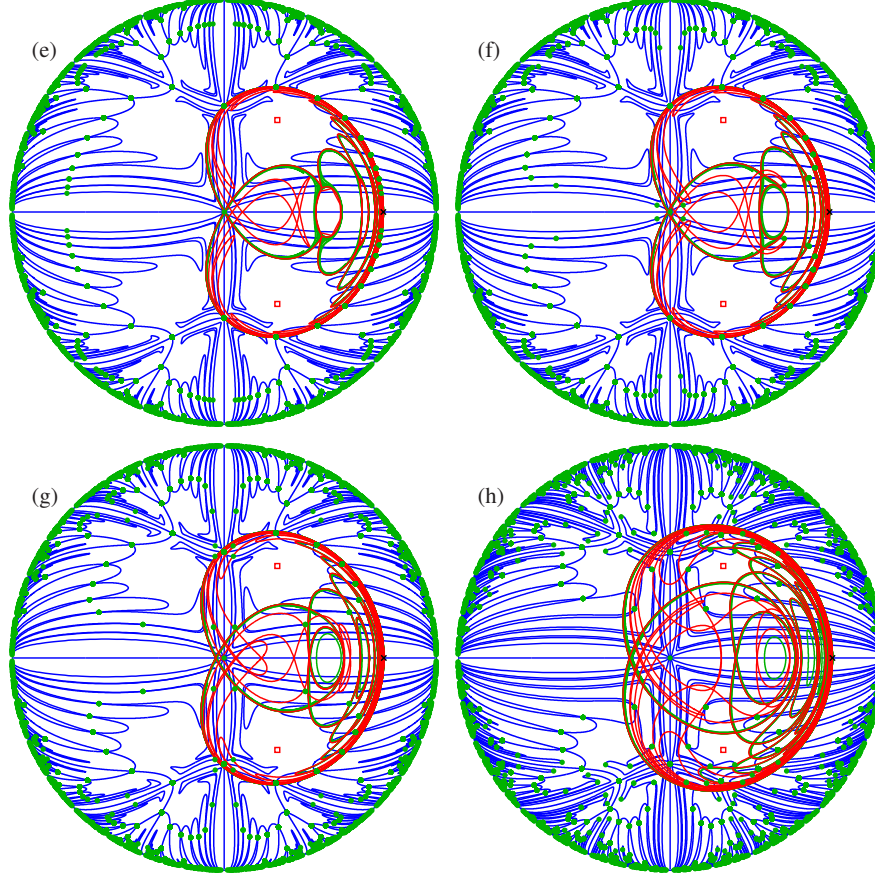


Fig. 6 continued The objects p , q^\pm , $W^s(p)$, $W^u(p)$, \mathcal{J}^- and \mathcal{J}^+ on the Poincaré disk; from (e) to (h) $a = \lambda$ take the values 0.76302, 0.765, 0.77 and 0.8.

these interactions with J_0 induce effects near J_1 and its images. As a result of this first backward critical tangency, $W^u(p)$ has points of self-intersection on each of its two branches (on top of the intersections between the two branches). Consider the region \mathcal{A} enclosed by the first segments of the two branches of $W^u(p)$ up to when they meet on the real line. Before the backward critical tangency all points of \mathcal{J}^- lie outside the region \mathcal{A} . In this and the accumulating further backward critical tangencies, more and more points of \mathcal{J}^- move inside this region; see also Figures 6(g) and (h) for $a = \lambda = 0.77$ and $a = \lambda = 0.8$, respectively. Moreover, the map (6) has a chaotic attractor in the region \mathcal{A} , which is the closure of the unstable set $W^u(p)$ and, hence, also contains p . Because the forward critical set \mathcal{J}^+ accumulates on $W^u(p)$, the first backward critical tangency is also accumulated in parameter space, on the side of larger $a = \lambda$, by infinitely many forward-backward critical tangencies.

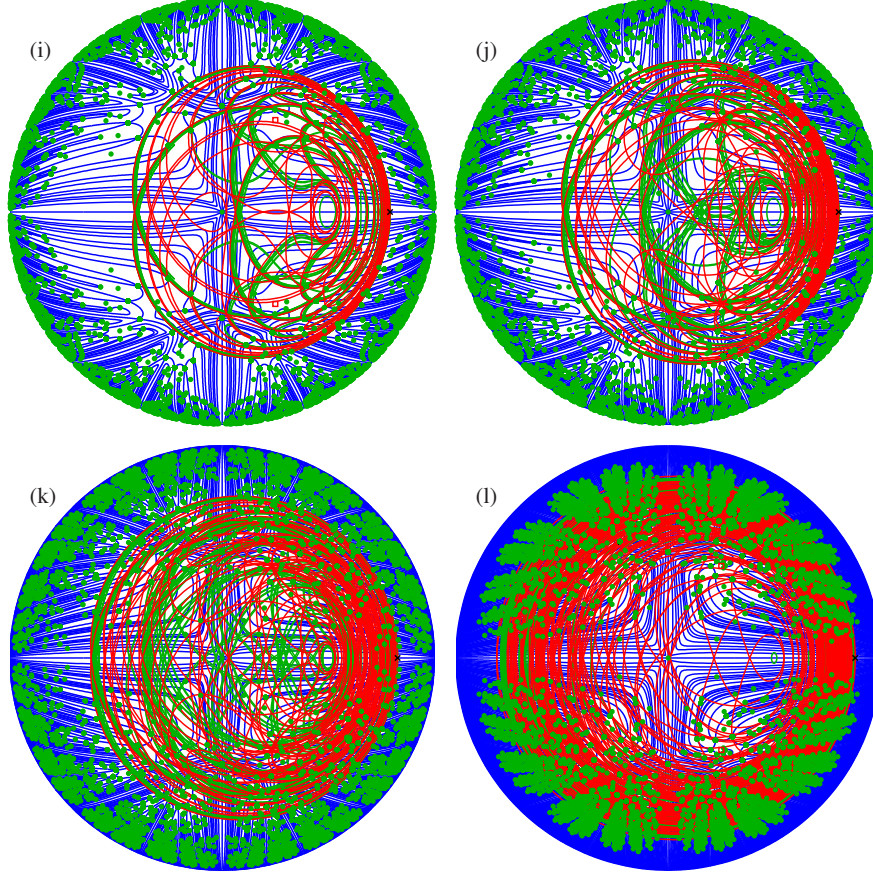


Fig. 6 continued The objects p , q^\pm , $W^s(p)$, $W^u(p)$, \mathcal{J}^- and \mathcal{J}^+ on the Poincaré disk; from (i) to (l) $a = \lambda$ take the values 0.85, 0.87, 0.9 and 0.95.

cies between \mathcal{J}^+ and \mathcal{J}^- . The forward-backward critical tangencies lead to the disappearance of certain sequences of backward orbits of J_0 from the backward critical set \mathcal{J}^- ; moreover, the closed curves in \mathcal{J}^+ develop self-intersections in the process. These effects of the forward-backward critical tangencies are difficult to discern in the phase portraits Figure 6(f)–(l); see [28] for details and illustrations.

When $a = \lambda$ is increased further, $W^u(p)$ and, thus, the region \mathcal{A} grows and incorporates more and more points of \mathcal{J}^- ; see Figure 6(i)–(k) for $a = \lambda = 0.85$, $a = \lambda = 0.87$ and $a = \lambda = 0.9$, respectively. At the same time, the sets $W^s(p)$, $W^u(p)$ and \mathcal{J} seem to become denser in the Poincaré disk, leading to ever more associated tangency bifurcations when $a = \lambda$ is increased. As Bamón, Kiwi, and Rivera-Letelier showed in [9], near $a = \lambda = 1$ the tangency bifurcations between stable and unstable sets of the hyperbolic saddle of (6) occur robustly. This mean

that there exists $0 << w^* < 1$, such that one finds a homoclinic tangency of the hyperbolic saddle for every point $(a, \lambda) \in (w^*, 1) \times (w^*, 1)$. We believe that Figure 6(l) for $a = \lambda = 0.95$ gives some impression of what wild chaos, that is, the robustness of homoclinic tangencies might look like. The saddle point p is only one of uncountably infinitely many nonwandering points; yet the sets $W^s(p)$ and $W^u(p)$ and the critical set \mathcal{J} already fill out the Poincaré disk increasingly densely.

3.2 The bifurcation diagram in the (a, λ) -plane

The bifurcations that are encountered as $a = \lambda$ is increased towards $a = \lambda = 1$ can be continued as curves when a and λ are allowed to vary independently. For tangency bifurcations this is done via the formulation of a suitable boundary value problem. These computations are based on the technique for continuing a locus of homoclinic tangency described in [10], which has been implemented in CLMatContM [18, 23]; details on how we adapted this method can be found in [28]. Figure 7 shows the resulting bifurcation diagram of (6) in the (a, λ) -plane; the points labelled (a)–(l) along the diagonal are the parameter points of the phase portraits of Figure 6. Starting from the lower-left corner, one first encounters the Neimark-Sacker bifurcation NS. The system then becomes chaotic when the curve H^0 of homoclinic tangency between $W^s(p)$ and $W^u(p)$ is crossed. As we already discussed, there are many more homoclinic tangencies that accumulate on H^0 and two of them are shown in Figure 7. These curves of secondary homoclinic tangencies turn around and cross the diagonal at least twice, between the points (c) and (d) and between the points (d) and (e); they each end on the curve B^0 of first backward critical tangency where $W^u(p)$ interacts with \mathcal{J}^- . Also shown in Figure 7 are five curves F^k of forward critical tangency between the primary manifold $W_0^s(p)$ and $f^{(k-1)}(J_1)$, namely, those for $k = 8, 10, 12, 14$ and 16 . Observe how each curve F^k passes very close to H^0 before turning away towards the right boundary of Figure 7 and note that F^k for $k = 12, 14$ and 16 cross the diagonal very close to the curve H^0 . The curve B^0 is accumulated by curves of further backward critical tangencies, for example, the curve B^2 . Figure 7 also shows the curve FB^{10} of forward-backward critical tangency between J_0 and $f^9(J_1)$, which lies very close to B^0 .

While the proof in [9] is valid only very close to the point $a = \lambda = 1$, the bifurcation diagram in Figure 7 suggests that one might expect to encounter wild chaos in a much larger region of the (a, λ) -plane. As soon as B^0 is crossed, infinitely many forward-backward critical tangencies have occurred, which are codimension-one homoclinic bifurcations of the equilibrium e of the five-dimensional Lorenz-type vector field; as such, they play the role of the homoclinic bifurcation in the Lorenz system (1). Apart from this geometric ingredient, the proof in [9] also requires that the parameters are such that (6) is area-expanding in a neighbourhood of the chaotic attractor. In [28] we conjecture that homoclinic tangencies occur robustly to the right of the first backward critical tangency B^0 ; this region is shaded in Figure 7. This is based on the suggestion that (6) is area-expanding in a neighbourhood of a subset of

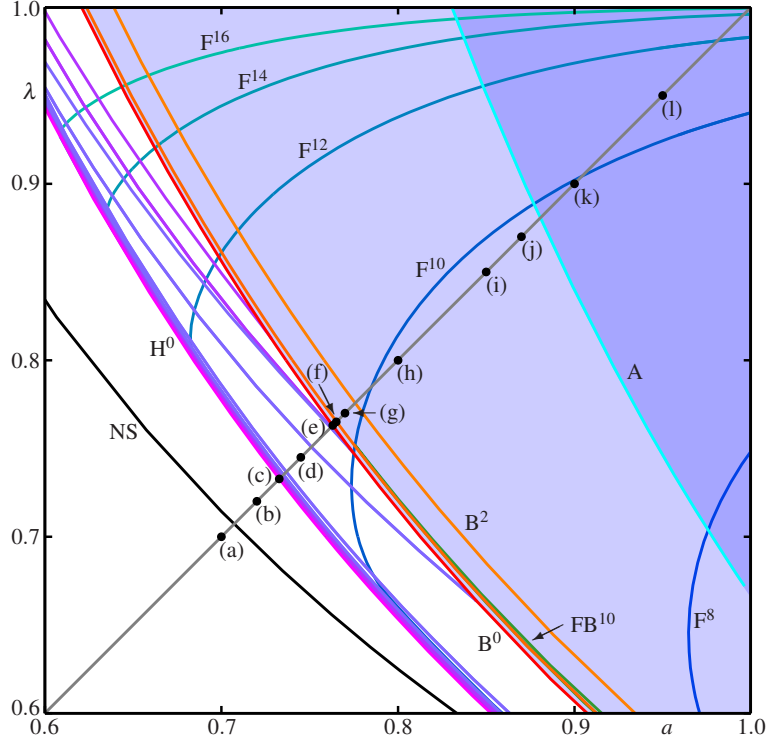


Fig. 7 Bifurcation diagram of (6) in the (a, λ) -plane for $a, \lambda \in \mathbb{R}$. Shown are the curve NS of Neimark-Sacker bifurcation of q^\pm , the curve H^0 of first homoclinic tangency and two further nearby curves of homoclinic tangency, the curves F^k for $k \in \{8, 10, 12, 14, 16\}$ of forward critical tangencies, the curve B^0 of first backward critical tangency and two further nearby backward critical tangencies (one of which is labelled B^2), the curve FB^{10} of forward-backward critical tangency, and the curve A (cyan) along which $\det(Df(p)) = 1$. The labelled points along the diagonal $a = \lambda$ correspond to the panels of Figure 6.

the attractor in this region. A sufficient (but not necessary) condition to ensure this area-expanding property is that the product of the eigenvalues of p exceeds 1. The curve A in Figure 7 is the locus where $\det(Df(p)) = 1$, and (6) is area-expanding in a neighbourhood of the chaotic attractor in the darker shaded region to the right of A. Hence, in this darker region wild chaos should certainly be expected. In particular, this means that the phase portraits of Figure 6(k) and (l), and possibly also those of Figure 6(g)–(j), are already from the regime of wild chaos.

4 Conclusions

We presented a geometric perspective of the techniques used to prove the existence of chaos in the Lorenz system (1). The same approach can also be applied to the study of wild chaos in higher-dimensional Lorenz-type vector fields. We focussed here on the two-dimensional noninvertible map (6) by Bámon, Kiwi and Rivera-Letelier [9] and discussed how interactions between its invariant objects are directly related to homoclinic and heteroclinic bifurcations of the associated five-dimensional Lorenz-type vector field. In this way, we were able to describe geometric changes in (6) during the transition from non-chaotic, via chaotic to wild chaotic dynamics. Our numerical results provide guidance for further theoretical study. In particular, we proposed the conjecture that the wild chaotic regime for (6) starts as soon as the first backward critical tangency bifurcation has occurred. Due to the accumulative nature of the respective objects, the first backward critical tangency induces infinitely many forward-backward critical tangencies, which emerge as a main ingredient for wild chaos. It remains to show that, in this regime, the attractor has the necessary area-expanding properties. The numerical methods we employed can be used to investigate other two-dimensional noninvertible maps and associated vector fields. In particular, it is of interest to explore possible routes to wild chaos in these other examples.

Acknowledgements The work on the Lorenz system presented here has been performed in collaboration with Sebius Doedel. We acknowledge his contribution to the computation of the Lorenz attractor as shown in Figure 1 and of the Lorenz manifold on the sphere in Figures 2 and 3; moreover, the leaves of the stable foliation in Figure 5 were computed with AUTO demo files that he developed recently. HMO and BK thank the organisers of ICDEA 2013 for their support, financial and otherwise.

References

1. Afraimovich, V. S., Bykov, V. V., Sil'nikov, L. P.: The origin and structure of the Lorenz attractor. *Sov. Phys. Dokl.* **22**, 253–255 (1977); translation from *Dokl. Akad. Nauk SSSR* **234**(2), 336–339 (1977)
2. Afraimovich, V. S., Bykov, V. V., Sil'nikov, L. P.: On structurally unstable attracting limit sets of Lorenz attractor type. *Trans. Mosc. Math. Soc.* **44**, 153–216 (1983)
3. Alligood, K. T., Sander, E., Yorke, J. A.: Crossing bifurcations and unstable dimension variability. *Phys. Rev. Lett.* **96**, 244103 (2006)
4. Alligood, K. T., Sauer, T. D., Yorke, J. A.: *Chaos — An Introduction to Dynamical Systems*. Springer-Verlag, New York (1996)
5. Aguirre, P., Doedel, E. J., Krauskopf, B., Osinga, H. M.: Investigating the consequences of global bifurcations for two-dimensional invariant manifolds of vector fields. *Discr. Contin. Dynam. Syst. — Ser. A* **29**(4), 1309–1344 (2011)
6. Asaoka, M.: Hyperbolic sets exhibiting C^1 -persistent homoclinic tangency for higher dimensions. *Proc. Amer. Math. Soc.* **136**, pp. 677–686 (2008)
7. Asaoka, M.: Erratum to “Hyperbolic sets exhibiting C^1 -persistent homoclinic tangency for higher dimensions.” *Proc. Amer. Math. Soc.* **138**, p. 1533 (2010)

8. Bunimovich, L. A., Sinai, J. G.: Stochasticity of the attractor in the Lorenz model. In: Gaponov-Grekhov, A. V. (ed.) *Nonlinear Waves*, pp. 212–226, Proceedings of Winter School, Nauka Press (1979)
9. Bamón, R., Kiwi, J., Rivera-Letelier, J.: Wild Lorenz like attractors. arXiv 0508045 (2006); available at <http://arxiv.org/abs/math/0508045>
10. Beyn, W.-J., Kleinkauf, J.-M.: The numerical computation of homoclinic orbits for maps. *SIAM J. Numer. Anal.* **34**, 1207–1236 (1997)
11. Bonatti, C., Díaz, L., Viana, M.: Dynamics beyond Uniform Hyperbolicity. A global geometric and probabilistic perspective. *Encyclopaedia Math. Sci.* **102**. Springer-Verlag, Berlin (2005)
12. Creaser, J., Krauskopf, B., Osinga, H. M.: α -flips in the Lorenz system. Preprint of The University of Auckland (2013)
13. Doedel, E. J.: AUTO-07P: Continuation and bifurcation software for ordinary differential equations. with major contributions from Champneys, A. R., Fairgrieve, T. F., Kuznetsov, Yu. A., Oldeman, B. E., Paffenroth, R. C., Sandstede, B., Wang, X. J., Zhang, C.; available at <http://cmvl.cs.concordia.ca/>
14. Doedel, E. J., Krauskopf, B., Osinga, H. M.: Global bifurcations of the Lorenz manifold. *Nonlinearity* **19**(12), 2947–2972 (2006)
15. Doedel, E. J., Krauskopf, B., Osinga, H. M.: Global invariant manifolds in the transition to preturbulence in the Lorenz system. *Indag. Math. (N.S.)* **22**(3–4), 222–240 (2011)
16. England, J. P., Krauskopf, B., Osinga, H. M.: Computing one-dimensional stable manifolds and stable sets of planar maps without the inverse. *SIAM J. Appl. Dyn. Syst.* **3**(2), 161–190 (2004)
17. England, J. P., Krauskopf, B., Osinga, H. M.: Bifurcations of stable sets in noninvertible planar maps. *Internat. J. Bifur. Chaos Appl. Sci. Engrg.* **15**(3), 891–904 (2005)
18. Ghaziani, R. K., Govaerts, W., Kuznetsov, Yu. A., Meijer, H. G. E.: Numerical continuation of connecting orbits of maps in Matlab. *J. Difference Equ. Appl.* **15**, 849–875 (2009)
19. Ghrist, R., Holmes, P. J., Sullivan, M. C.: *Knots and Links in Three-Dimensional Flows*. Lecture Notes in Math. **1654**. Springer-Verlag, Berlin (1997)
20. Gilmore, R., Lefranc, M.: *The Topology of Chaos: Alice in Stretch and Squeeze Land* Wiley-Interscience, New York (2004)
21. Gonchenko, S. V., Ovsyannikov, I. I., Simó, C., Turaev, D.: Three-dimensional Hénon-like maps and wild Lorenz-like attractors. *Internat. J. Bifur. Chaos Appl. Sci. Engrg.* **15**, 3493–3508 (2005)
22. Gonchenko, S. V., Shilnikov, L. P., Turaev, D.: On global bifurcations in three-dimensional diffeomorphisms leading to wild Lorenz-like attractors. *Regul. Chaotic Dyn.* **14**, 137–147 (2009)
23. Govaerts, W., Kuznetsov, Yu. A., Ghaziani, R. K., Meijer, H. G. E.: CL_MatContM: a toolbox for continuation and bifurcation of cycles of maps (2008) Available via <http://sourceforge.net/projects/matcont>
24. Guckenheimer, J.: A strange strange attractor. In: Marsden, J. E., McCracken, M. (eds.) *The Hopf Bifurcation and its Applications*, pp. 368–382. Springer-Verlag, New York, Heidelberg, Berlin (1976)
25. Guckenheimer, J., Holmes, P.: *Nonlinear Oscillations, Dynamical Systems and Bifurcations of Vector Fields*. Springer-Verlag, New York, 2nd edition (1986)
26. Guckenheimer, J., Williams, R. F.: Structural stability of Lorenz attractors. *Publ. Math. IHES* **50**, 59–72 (1979)
27. Hénon, M.: A two-dimensional mapping with a strange attractor. *Commun. Math. Phys.* **50**(1), 69–77 (1976)
28. Hittmeyer, S., Krauskopf, B., Osinga, H.M.: Interacting global invariant sets in a planar map model of wild chaos. *SIAM J. Appl. Dyn. Syst.* **12**(3), 1280–1329 (2013)
29. Kaplan, J. L., Yorke, J. A.: Preturbulence: A regime observed in a fluid flow model of Lorenz. *Commun. Math. Phys.* **67**, 93–108 (1979)
30. Krauskopf, B., Osinga, H.M.: Computing geodesic level sets on global (un)stable manifolds of vector fields. *SIAM J. Appl. Dyn. Syst.* **2**(4), 546–569 (2003)

31. Krauskopf, B., Osinga, H.M.: Computing invariant manifolds via the continuation of orbit segments. In: Krauskopf, B., Osinga, H.M., Galán-Vioque, J. (eds.) *Numerical Continuation Methods for Dynamical Systems*, pp 117–154. Underst. Complex Syst. Springer-Verlag, New York (2007)
32. Krauskopf, B., Osinga, H.M., Peckham, B. B.: Unfolding the cusp-cusp bifurcation of planar endomorphisms *SIAM J. Appl. Dyn. Syst.* **6**(2), 403–440 (2007)
33. Krauskopf, B., Osinga, H.M., Doedel, E.J., Henderson, M. E., Guckenheimer, J., Vladimírsky, A., Dellnitz, M., Junge, O.: A survey of methods for computing (un)stable manifolds of vector fields. *Internat. J. Bifur. Chaos Appl. Sci. Engrg.* **15**(3), 763–791 (2005)
34. Kuznetsov, Yu. A.: *Elements of Applied Bifurcation Theory*. Springer-Verlag, New York, 2nd edition (1998)
35. Lorenz, E. N.: Deterministic nonperiodic flows. *J. Atmosph. Sci.* **20**, 130–141 (1963)
36. Moreira, C. G.: There are no C^1 -stable intersections of regular Cantor sets. *Acta Math.* **206**, 311–323 (2011)
37. Newhouse, S. E.: The abundance of wild hyperbolic sets and nonsmooth stable sets for diffeomorphisms. *Publ. Math. IHES* **50**(1), 101–151 (1979)
38. Palis, J., de Melo, W.: *Geometric Theory of Dynamical Systems*. Springer-Verlag, New York (1982)
39. Palis, J., Takens, F.: *Hyperbolicity & Sensitive Chaotic Dynamics at Homoclinic Bifurcations*. Cambridge University Press, Cambridge (1993)
40. Perelló, C.: Intertwining invariant manifolds and Lorenz attractor. In: *Global theory of dynamical systems*. Proc. Internat. Conf., Northwestern Univ., Evanston, Ill., 1979, pp. 375–378. *Lecture Notes in Math.* **819**. Springer-Verlag, Berlin (1979)
41. Rand, D.: The topological classification of Lorenz attractors. *Math. Proc. Cambridge Philos. Soc.* **83**, 451–460 (1978)
42. Robinson, C.: *Dynamical Systems: Stability, Symbolic Dynamics, and Chaos*. CRC Press LLC, Boca Raton, Florida, 2nd edition (1999)
43. Sparrow, C.: *The Lorenz Equations: Bifurcations, Chaos and Strange Attractors*. Appl. Math. Sci. No. **41**. Springer-Verlag, New York (1982)
44. Sinai, J. G., Vul, E. B.: Hyperbolicity conditions for the Lorenz model. *Physica D* **2**, 3–7 (1981)
45. Tucker, W.: The Lorenz attractor exists. *C. R. Acad. Sci. Paris Sér. I Math.* **328**(12), 1197–1202 (1999)
46. Turaev, D. V., Shilnikov, L. P.: An example of a wild strange attractor. *Mat. Sb.* **189**, 291–314 (1998)
47. Turaev, D. V., Shilnikov, L. P.: Pseudo-hyperbolicity and the problem on periodic perturbations of Lorenz-like attractors. *Russian Dokl. Math.* **77**, 17–21 (2008)
48. Williams, R. F.: The structure of Lorenz attractors. *Publ. Math. IHES* **50**, 101–152 (1979)
49. Zhang, W., Krauskopf, B., Kirk, V.: How to find a codimension-one heteroclinic cycle between two periodic orbits. *Discrete Contin. Dyn. Syst. Ser. A* **32**(8) pp. 2825–2851 (2012)